THE JOURNAL OF PHYSICAL CHEMISTRY LETTERS
A JOURNAL OF THE AMERICAN CHEMICAL SOCIETY

pubs.acs.org/JPCL
Letter

Electron Diffusion Length Effect on Direction of Irradiance in Transparent $FAPbBr_3$ Perovskite Solar Cells

Published as part of The Journal of Physical Chemistry Letters special issue "Optoelectronic Characterization of Halide Perovskites and Organic Devices".

Osbel Almora,* Farshad Jafarzadeh, Mohamed Samir, Renán Escalante, Diego Di Girolamo, Jessica Barichello, Francesca Brunetti, Lluis F. Marsal, Fabio Matteocci,* and Juan Antonio Anta*

Cite This: J. Phys. Chem. Lett. 2024, 15, 10153−10161

Read Online

ACCESS | Metrics & More | Article Recommendations | Supporting Information

ABSTRACT: Transparent photovoltaics for building integration represent a promising approach for renewable energy deployment. These devices require transparent electrodes to manage transmittance and to ensure proper cell operation. In this study, transparent $FAPbBr_3$-based perovskite solar cells optimized via a passivation treatment were demonstrated with average visible transmittance values above 60% and light utilization efficiencies up to 5.0%. Experiments under varying ultraviolet (UV) irradiance intensities from both front and rear directions revealed performance differences correlated with diffusion-limited transport and open-circuit voltage changes. Combining the UV-radiated experiments and drift-diffusion simulations, an asymmetry between the diffusion lengths of electrons and holes in the perovskite is revealed, with estimated values resulting in less than 50 nm and more than 99 nm, respectively. Our methods not only identify electron−hole diffusion length differences but also introduce a general protocol for characterizing solar cells with transparent electrodes.

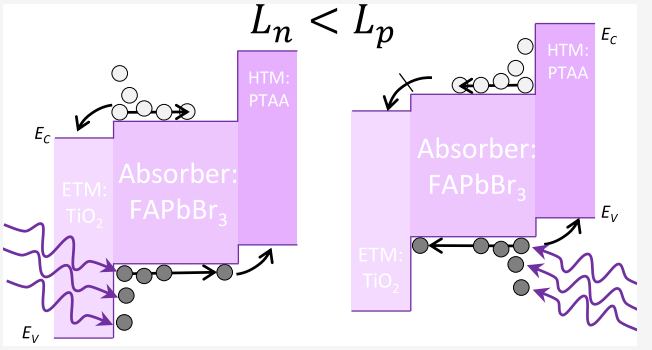

Emerging thin film photovoltaics (PVs)[1] can be designed to use transparent electrodes, and thin absorber layers whose bandgap energy (E_g) can be engineered to absorb a fraction of the incident irradiance and transmit a significant part.[2,3] This marks a significant difference from the established PV technologies, such as crystalline silicon, where the thick wafers and the E_g invariability hinder the transparency of the devices. Transparent and semitransparent PVs promise opportunities for building integration, such as solar windows and facades,[4−6] agrivoltaics,[7,8] and indoor applications.[9,10] More recently, the advent of transparent luminescent solar concentrators has also been proposed.[11] However, the device performance and the color tunability of these devices continues to be challenging.

Current state-of-the-art research[1] shows significant progress among transparent and semitransparent perovskite solar cells (PSCs), which not only shows perspective for building integration[6] but also paves the way for the development of tandem photovoltaics,[12] space technology, and the Internet of Things.[13]

Formamidinium lead bromide ($FAPbBr_3$) is a perovskite absorber with a large bandgap ($E_g \approx 2.28$ eV) which intrinsically transmits more than half of the visible range spectrum (VIS) and can theoretically reach up to 30% efficiency in tandem configuration with a bottom subcell of $E_g \approx 1.6$ eV (e.g., $MAPbI_3$). $FAPbBr_3$-based PSCs have achieved efficiencies exceeding 10% in opaque devices[14] and 8% in semitransparent devices.[15] Specifically, the use of quaternary ammonium halides has demonstrated improvements in performance and long-term stability for these devices.[16,17] The lead content in $FAPbBr_3$ may raise questions on its suitability.[18,19] However, not only have several encapsulation and recycling strategies already been identified and continue to be under research for mitigating environmental and health impacts[20,21] but also the perovskite layer in transparent PSCs is typically thinner, which reduces the lead quantity.

The thinner the absorption layer, the higher its transmittance ($\mathbb{T}$), leaving aside interference and diffraction phenomena. For transparent PV applications, the focus is set on the visible region of the spectra (VIS), which is characterized by the photopic response of the human eye

Received: August 11, 2024
Revised: September 20, 2024
Accepted: September 24, 2024
Published: September 30, 2024

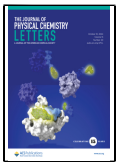

https://doi.org/10.1021/acs.jpclett.4c02364
J. Phys. Chem. Lett. 2024, 15, 10153−10161

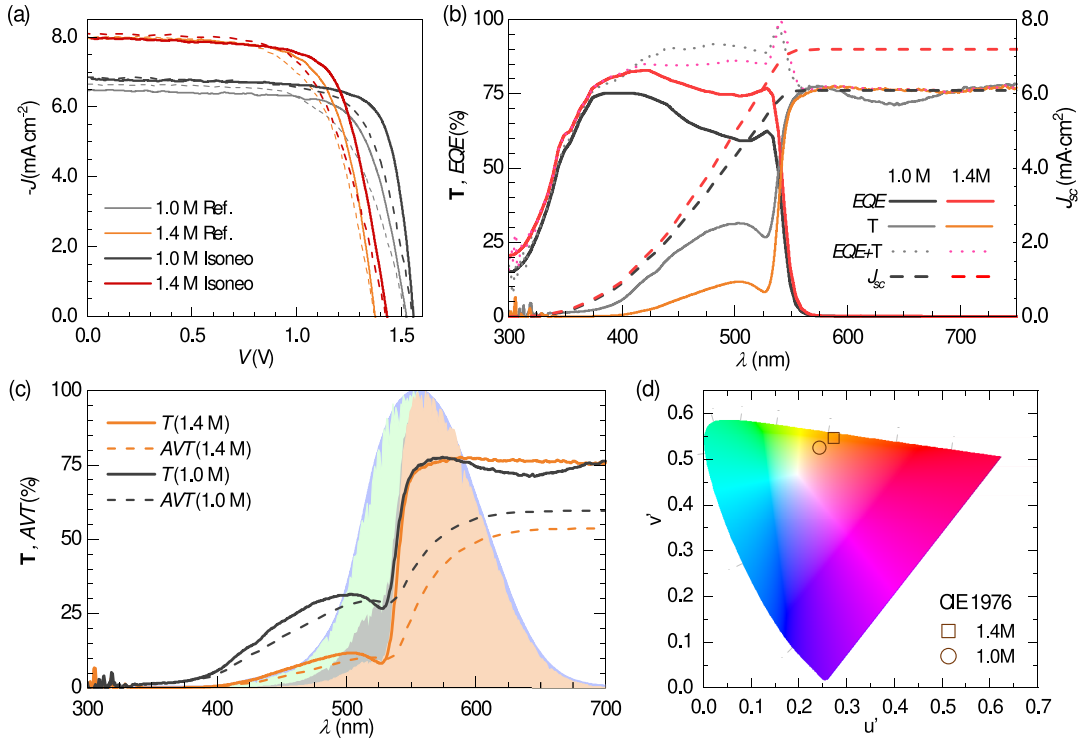

Figure 1. Optoelectronic characterization of the 1 and 1.4 M samples with and without Isoneo passivation in the front direction of illumination. (a) Illustrative $J-V$ curves under 1 sun illumination; forward and reverse bias scan (100 mV s^{-1}) directions are indicated with dashed and solid lines, respectively. The *EQE* spectra for passivated samples are shown in b, and the corresponding transmittance spectra are in b and c. The right axis and dashed lines in (b) indicate the integrated short-circuit current for $\Gamma_{AM1.5G}$. The dotted lines in b represent the PBCC of eq 5. In c, the dashed lines illustrate the *AVT* integral of eq 1; the blue and green areas correspond to Γ_P and $\Gamma_P{\cdot}\Gamma_{AM1.5G}$, respectively; and the gray and orange areas indicate $\mathbb{T}{\cdot}\Gamma_P{\cdot}\Gamma_{AM1.5G}$ for the 1.0 and 1.4 M samples, respectively. The sample color is illustrated in d with the corresponding chromaticity coordinates, and pictures can be found in Figure S3.

(Γ_P). Therefore, the relevant parameter to consider is the average visible transmittance:[22]

$$AVT = \frac{\int \mathbb{T}(\lambda)\Gamma_P(\lambda)\Gamma_{AM1.5G}(\lambda)\,d\lambda}{\int \Gamma_P(\lambda)\Gamma_{AM1.5G}(\lambda)\,d\lambda} \quad (1)$$

where $\Gamma_{AM1.5G}(\lambda)$ is the solar spectrum photon flux and the integrals over the wavelength (λ) values between zero and infinity are actually reduced to the visible light range. Ideally, the transparent PV devices would transmit all of the incident photon flux with energies within the visible range and smaller than that of E_g, whereas the remaining photons would be absorbed. In practice, the obtention of convenient transmittance spectra is challenging and the overall absorptance ($\mathbb{A}$) of the device is reduced as $\mathbb{T}$ increases. For an incident photon power density (P_{in}), the higher the $\mathbb{T}$, the smaller the charge carrier generation and thus the electric output power density (P_{out}), leading to a reduced power conversion efficiency

$$PCE = \frac{P_{out}}{P_{in}} = \frac{J_{sc}V_{oc}FF}{P_{in}} \quad (2)$$

where J_{sc} is the short-circuit density; V_{oc}, the open-circuit voltage; and *FF*, the fill factor. Therefore, a trade-off is considered between the *AVT* and the *PCE*, which can be linearly balanced with the definition of the light utilization efficiency[23]

$$LUE = PCE{\cdot}AVT \quad (3)$$

Equation 3 quantifies the overall performance of transparent and semitransparent solar cells in a way that, for each *AVT*, the higher the *PCE* the better. This leads back to the fundamental study case in PVs: the reduction of energy losses, either optical or electrical.

Optical losses in transparent devices arise mainly from reflectance ($\mathbb{R}$) and parasitic $\mathbb{T}$ out of the VIS. Notably, the bifacial[24] functionality of transparent devices not only enhances the versatility of device applications but also indicates the extent to which the optical losses are relevant. Differences between front and rear $\mathbb{T}$ and/or $\mathbb{A}$ spectra suggest optical issues with transparent electrodes and absorber layers. However, it can be the case where small optical losses cannot explain larger performance differences due to electrical losses when comparing device operation in front and rear irradiance.

The reduction of electrical losses due to nonradiative recombination is arguably the most challenging aspect in the optimization of solar cells. This relates to the difficulty to identify the location of the recombination centers (e.g., trap defects in the bulk or at the interfaces), their nature, and the strategies to mitigate their effects. Most typically, the Shockley–Read–Hall (SRH) recombination is approached in the time domain via the transient spectroscopic experiments for estimating the recombination lifetime for electrons (τ_n) and holes (τ_p), i.e., the effective time from charge carrier generation until recombination event. However, in the space domain, it is the diffusion length that provides the analogous definition: the average distance a photogenerated charge carrier can diffuse before a recombination event occurs. Importantly, the

https://doi.org/10.1021/acs.jpclett.4c02364
J. Phys. Chem. Lett. 2024, 15, 10153−10161

Einstein's relation[25] can be used to relate the electron and holes diffusion coefficients for electrons (D_n) and holes (D_p). Then, the diffusion lengths for electrons and holes can be approached[26] to

$$L_n = \sqrt{\tau_n D_n} \tag{4a}$$

and

$$L_p = \sqrt{\tau_p D_p} \tag{4b}$$

respectively, where a direct squared root relation is expected with the lifetimes. Therefore, estimating the diffusion lengths informs both the time and space "life spans" of charge carriers. However, in practice, most of the methods for estimating $L_{n,p}$ follow eq 4 and individually assess the lifetime and the diffusion coefficients throughout the mobility.[27] This is already controversial, since the techniques employed for each experiment do not necessarily relate to the same variety of phenomena. For instance, bulk or interface contributions can be neglected in one technique or the other, depending on the time scale and/or the location of the perturbation in the sample and the corresponding signal.[28] Interestingly, Halme et al.[29] performed intensity modulated photocurrent experiments with dye-sensitized solar cells and found different responses for each direction of illumination; i.e., electrode and electrolyte, demonstrating that an important correlation between the directionality of illumination and diffusion exists when diffusion lengths are on the order of the active layer thickness and the photon absorption penetration lengths are relatively small.

In this work, transparent TiO_2/$FAPbBr_3$/PTAA PSCs with different absorber layer thicknesses and fabrication methods are characterized, and a methodology for assessment of diffusion-limiting transport is introduced. The optoelectronic properties of devices with different thicknesses are established by studying the current density−voltage (J−V) curve, the external quantum efficiency (EQE),[30] and the $\mathbb{T}$ spectra. Moreover, the different sample thicknesses are confirmed via electron scanning microscopy (SEM) images and $\mathbb{A}$ spectra. Importantly, the open circuit−voltage, impedance spectroscopy (IS),[31] and intensity modulated photocurrent (IMPS)[32] and photovoltage (IMVS)[33] spectroscopies are explored with front and rear ultraviolet (UV) irradiance. These measurements are correlated with drift-diffusion (DD) simulations and empirical analytical expressions that introduce a method for assessing the differences in perovskite bulk diffusion lengths between electrons and holes. The proposed protocol can be applied to any solar cell with transparent electrodes.

The device performance characterization of the studied samples is presented in Figure 1, and further details on device fabrication and measurement methods can be found in sections S1.1 and S1.2, respectively, in the Supporting Information. Four main sample types were analyzed attending to the thickness, passivation method, and perovskite layer thickness. The reference (ref) samples were exempted of passivation, and the Isoneo samples are those including the interfacial passivation treatment.[13] Moreover, each type of cell (with/without passivation) was also fabricated with two different concentrations of the precursor solution, 1 and 1.4 M, which resulted in thickness variation of the absorber layer.

The J−V curves under 1 sun illumination are presented in Figure 1a including bias voltage sweeps in both forward (FW, from short-circuit to open-circuit) and reverse (RV, from open-circuit to short-circuit) directions, with an scan rate of 100 mV·s^{-1}, accounting for the hysteresis.[34] The PCE results were similar for the four sample types, around 7%, with slightly higher values for the 1.4 passivated devices (see Table S1). Notably, the V_{oc} values are practically independent of the scan rate direction, whereas the J_{sc} and the FF are affected to some extent by the direction in which the voltage is swept. This agrees with the cumulative statistical data in Figure S1, in the Supporting Information, where the evaluation of the stability of the samples is also illustrated under several test conditions.

Modifying the thickness involves a trade-off between the photocurrent and the photovoltage. Within an optimal range, a thinner sample results in a smaller fraction of absorbed photon flux, leading to a lower generation of charge carriers and, thus, a reduced photocurrent. However, varying the thickness can also alter the morphology and, subsequently, the concentration of recombination sites.

The photocurrent reduction due to the decrease in the thickness of the perovskite layer is also evident in the EQE spectra of Figure 1b. The passivated 1.4 M sample shows higher ratios of incident-photons-to-current efficiencies with respect to the 1.0 M sample, resulting in higher values of the integrated J_{sc}, as shown in the right axis of Figure 1b (dashed lines). Importantly, the EQE spectra were further tested with respect to the $\mathbb{T}$ spectra in terms of the photon balance consistency check:[22]

$$PBCC = EQE + \mathbb{T} < 1 \tag{5}$$

as presented in Figure 1b with dotted lines. The higher the EQE values, the smaller those of the $\mathbb{T}$, but in all cases the summation of the spectra does not exceed unity (100%). Only in the absorption threshold does the $PBCC$ approach unity, meaning that reflectance ($\mathbb{R}$) and any further dissipation mechanisms are minimal, if not zero, near the wavelength corresponding to E_g. Notably, the photovoltaic bandgap[30] of the fabricated $FAPbBr_3$-based devices resulted in E_g = 2.28 eV, as defined by the derivative of the EQE spectra[30,35] in Figure S2, in the Supporting Information.

The integrated AVT spectra are included in Figure 1c, as well as the corresponding $\mathbb{T}$, the Γ_P spectrum, and the subsequent steps in the integration process of eq 1. First, the total Γ_P spectrum is indicated with the blue area, and the green area represents the product $\Gamma_P \cdot \Gamma_{AM1.5G}$. Then, the gray and orange areas signify the $\mathbb{T}\cdot\Gamma_P\cdot\Gamma_{AM1.5G}$ products for the 1.0 and 1.4 M passivated samples, resulting in AVT values of 59.6% and 53.6%, respectively. These AVT values can be substituted in eq 3 to obtain LUE values as high as 5.0%. Furthermore, from the apparent reflectance (see $\mathbb{R} < (1 - EQE - \mathbb{T})$ in Figure 1b) and the clearly transmitted section of the VIS (see Figure 1c), an orangish color for the samples is evident. This is illustrated in the calculation of the uniform chromaticity coordinates (CIE 1976) in Figure 1d and the photographs in Figure S3a. Additionally, the color rendering index (CRI)[22] resulted in values of 70 and 45.6, for the 1.0 M and the 1.4 M samples, respectively (see details on CRI in section S1.2).

The layer-by-layer structure and optical properties of the samples were also investigated, as summarized in Figure S3b−f, in the Supporting Information. The SEM cross-section images in combination with the analyses of $\mathbb{T}$, $\mathbb{R}$, $\mathbb{A}$, and the effective uniform absorption coefficient (α) spectra of the 1.0 and 1.4 M samples suggest effective thicknesses (L) of approximately 150 and 255 nm, respectively. Importantly, the estimation of α

https://doi.org/10.1021/acs.jpclett.4c02364
J. Phys. Chem. Lett. 2024, 15, 10153−10161

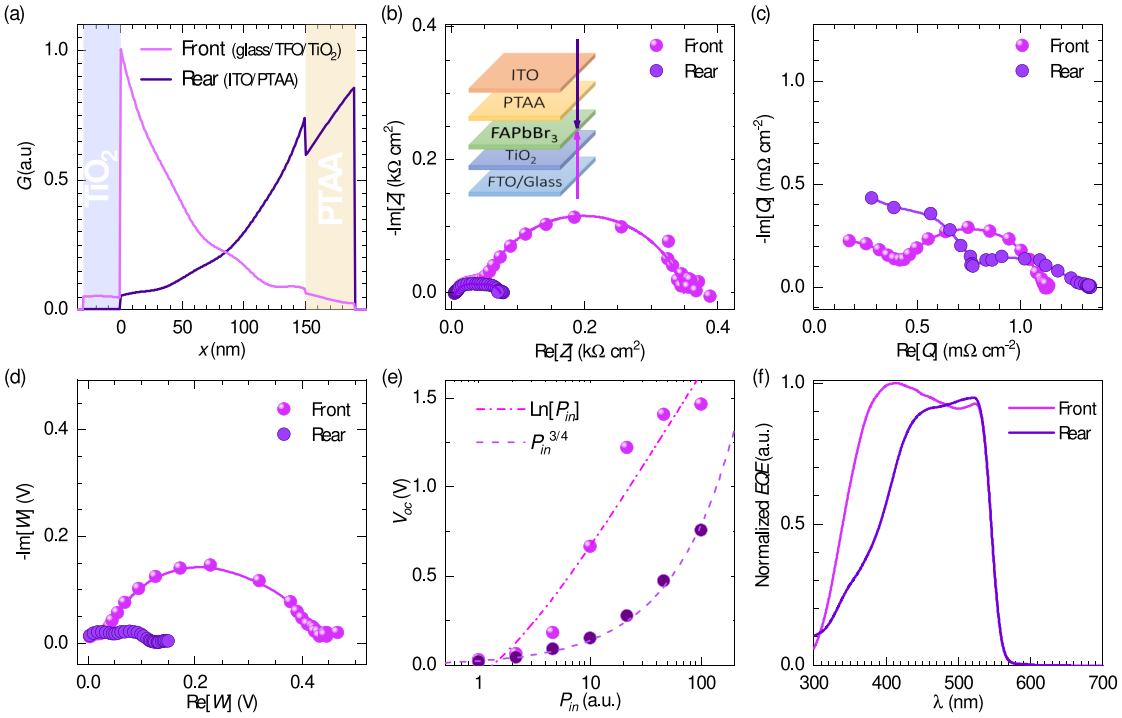

Figure 2. Front and rear directions of UV irradiance, as indicated: (a) simulated charge carrier generation rate for incident 365 nm photons into the 1.0 M sample; illustrative experiments with Isoneo 1.4 M samples including (b) IS, (c) IMPS, and (d) IMVS spectra under (quasi-) open-circuit conditions for the highest UV irradiance intensities; (e) DC open-circuit voltage as a function of normalized incident power densities; and (f) *EQE* spectra. The inset in b illustrates the layer-by-layer structure of the samples.

follows the Beer−Lambert (B-L) law,[36] which gives the position x-dependent monochromatic photon flux

$$\Gamma(x, \lambda) = \Gamma(0, \lambda) \exp[-\alpha(\lambda)x] \quad (6)$$

for an incident monochromatic flux $\Gamma(0, \lambda)$ of photons just inside the surface of the material (i.e., after accounting for reflection), with wavelength λ. Moreover, the B-L law introduces the useful concept of photon penetration length or effective charge carrier generation region of width $w = 1/\alpha$. Particularly, the studied $FAPbBr_3$ layers showed $w < 100$ nm for $\lambda < 400$ nm (see Figure S3f). This suggests that UV irradiance would be totally absorbed in the perovskite layers within regions smaller than their thicknesses ($w_{UV} < L$), in agreement with the negligible $\mathbb{T}$ spectra for the 1.4 M sample in Figure 1c,d.

Some performance differences between the samples can also be identified from IS measurements in quasi-open-circuits under different white LED illumination intensities. The experimental spectra were fitted to the equivalent circuit in Figure S4, and the resulting analyses are summarized for the 1.0 and 1.4 M samples in Figures S5 and Figure S6, in the Supporting Information, respectively. In general, higher resistance (R) can be identified for the passivation-treated devices with respect to the nonpassivated ones. This suggests an increase in the recombination resistance for the Isoneo samples, whose nonradiative recombination may have been reduced. The capacitance (C) showed a drastic decrease for the passivated sample with respect to the reference among the 1.0 M devices but nearly unchanged spectra for the 1.4 M samples. These features may be related to the competition between geometric capacitances from the perovskite layer and those of the selective contacts and interfaces.

The passivated samples were further studied by means of alternating-current mode (AC) techniques including IS, IMPS, and IMVS spectra in (quasi-) open-circuit conditions under different irradiance intensities. However, in order to probe the impact of the recombination and the diffusion lengths, in this case, the illumination was provided by a 365 nm monochromatic UV-LED (PAIOS Fluxim), and a comparison was made between the front and rear directions of irradiance, herein defined as those where the photon flux is interacting with the glass/FTO/TiO_2 and ITO/PTAA layers before the perovskite, respectively. This front/rear distinction is graphically illustrated in the simulated charge carrier generation rate (G) profile in Figure 2a (SETFOS Fluxim, see section S2 in the Supporting Information) and the layer-by-layer inset diagram in Figure 2b.

The IS characterization of a passivated (thinner) 1.0 M sample in quasi-open-circuit under different UV irradiance intensities shows similar spectra for both front and rear directions of radiance, as presented in Figure S7, in the Supporting Information. This agrees with the G profile in Figure 2a, since the perovskite layer thickness (~150 nm) is close to the photon penetration length. Moreover, the equivalent circuit modeling (Figure S4) was employed to obtain the C, R, and τ summarized in Figure S8a−c, respectively, in the Supporting Information. These parameters reproduce a similar behavior with a slight increase in C and R (and subsequently τ) for the front illumination. Furthermore, the V_{oc} values as a function of the incident illumination intensities, and the *EQE* spectra are also presented in Figure S8d,e, confirming the effective similarity between the electrical response of the sample in both directions of illumination for the (thinner) 1.0 M sample.

https://doi.org/10.1021/acs.jpclett.4c02364
J. Phys. Chem. Lett. 2024, 15, 10153−10161

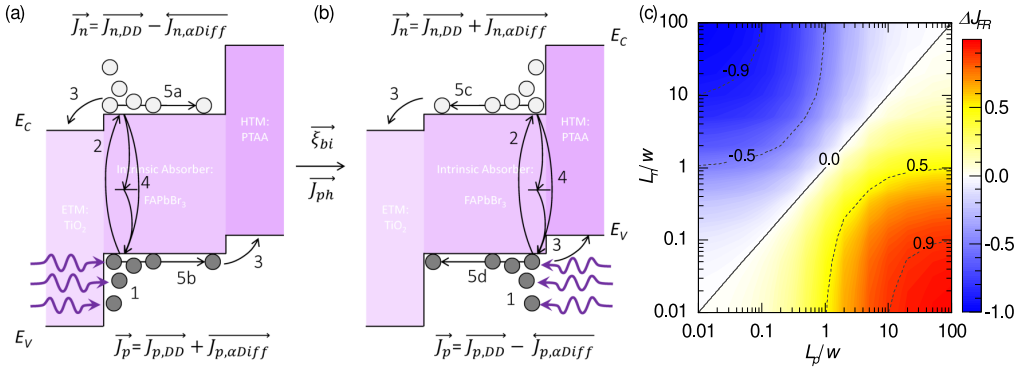

Figure 3. Illustrative energy diagram for a TiO_2/$FAPbBr_3$/PTAA solar cell with transparent electrodes under monochromatic UV irradiation from the (a) front (ETM: TiO_2) and (b) rear (HTL: PTAA) electrodes and (c) normalized direction current difference of eq 9. Main processes include (1) photon absorption, (2) charge carrier generation, (3) charge extraction through drift and diffusion toward the selective contacts, and (4) recombination, in the diagram. When photon penetration length is smaller than the thickness of the absorber layer ($w < L$), B-L absorption-related (5) diffusion of charge carriers occur. In (a) front irradiation, (5a) electrons and (5b) holes diffuse toward the HTL, whereas for (b) rear irradiance, (5c) electrons and (5d) holes diffuse toward the ETL. In between the two diagrams, the direction of built-in field and photocurrent is indicated.

A thicker (1.4 M) passivated sample was also explored via IS in quasi-open-circuit conditions under different UV illumination intensities, as shown in Figure S9 and summarized in Figure 2b–d. However, unlike the thinner sample, in this case clear differences were obtained when comparing front and rear irradiance directions. For instance, the impedance (Z) Nyquist plot from IS measurements at the highest UV direct-current mode (DC) irradiance intensity in Figure 2b illustrates a significant increase of resistance (R) for the front illumination with respect to that of the rear irradiance. This difference is significantly dependent on the irradiance intensity, as shown in Figure S10.

The photocurrent and photovoltage responsivities, Q and W, from IMPS and IMVS are presented in Figure 2c,d, respectively, and for analogue DC conditions to those of the IS in Figure 2b. Two characteristic semicircles are evident in all spectra in Nyquist plot representation, but it is the higher photovoltage W response in the front direction of irradiance, with respect to the rear one, that marks the main contribution to the resistance ($Z = W/Q$).[33] In addition, a clear resemblance is found between the IMVS spectra and the corresponding spectra from the IS measurements. This not only validates the consistency of the measurement protocol[32] but also suggests the recombination nature of the resistance in quasi-open-circuit conditions.[37]

The DC measurements of V_{oc} as a function of the incident UV irradiance intensity (Figure 2e) reveal higher photovoltage values when irradiated from the front compared with the rear. The higher the intensity of irradiance, the higher the difference in V_{oc} values, although a saturation of the trend is also observed for the highest UV intensities. While the front V_{oc} shows the typical logarithm increase with the P_{in}, the rear one apparently follows a 3/4-power law. This suggests potential UV-activated phase transitions modifying transport parameters with rear irradiance, whose full comprehension is beyond the scope of this manuscript. More importantly, the consistent observation of significantly higher V_{oc} values in the front compared to the rear direction of irradiance cannot be solely related to the higher charge carrier generation (Figure 2a). Therefore, higher recombination lifetimes appear for the front compared to the rear direction, accounting for the results from both the AC and DC experiments in open-circuit conditions (Figure 2b–e).

The DC EQE spectra in short-circuit conditions are presented in Figure 2f, comparing the effect of different directions of irradiance. Unlike the thinner 1.0 M sample (see Figure S8), the 1.4 M device shows a clear reduction in the spectrum from the rear when compared to front as the wavelength approaches the UV range, for $\lambda < 400$ nm. Since short-circuit conditions favor transport over recombination, the higher photocurrent responsivity in the front direction can be associated with transport differences in diffusion lengths rather than solely recombination lifetimes, as one may conclude from the experiments conducted under open-circuit conditions (Figure 2b–e).

The understanding of our experiments was contrasted with DD simulations (see section S2 in the Supporting Information). First, the increase of J_{sc} and decrease of V_{oc} in the J–V curves in Figure 1a, as the thickness L of the perovskite layer increased from the 1.0 M to the 1.4 M samples, is qualitatively reproduced in Figure S11. This served as a calibration for the simulation parameters in Table S3 and also indicated a decrease of bulk recombination lifetime for the thicker perovskite layer compared to the thinner one, possibly due to a higher concentration of bulk recombining traps.

Second, several simulations were conducted to reproduce a difference in electrical response between front and rear directions of irradiance, given the absorption coefficient of a 255-nm-thick $FAPbBr_3$ layer (see Figure S3). This included three main hypotheses for the imbalance of the electrical response: (i) changes in recombination velocities at the interfaces, (ii) ion-mediated phenomena, and (iii) differences in L_n and L_p in the bulk of the perovskite. None of the explored ranges of simulation parameters within the framework of SETFOS-Fluxim reported significant electrical response differences between front and rear directions of irradiance for hypotheses i and ii. In contrast, it was only with the assumption of $L_n \ll L_p$ that the current, recombination resistance, and photovoltage resulted in higher values in the front compared to the rear direction of UV irradiance. For instance, Figure S12 illustrates the qualitative reproduction of the experimental trends for the IS spectra and V_{oc}–P_{in} in the front and rear directions of UV irradiance. Particularly, our best qualitative agreement between experiments and simu-

https://doi.org/10.1021/acs.jpclett.4c02364
J. Phys. Chem. Lett. 2024, 15, 10153–10161

lations was obtained for the diffusion lengths of electrons and holes in the ranges of $L_n < 50$ nm and $L_p > 99$ nm, respectively.

Notably, it could be argued that the directional effect could be due to the parasitic absorption of the contacts, e.g., the PTAA (see Figure 2a). However, the stronger decrease of V_{oc} with rear irradiance from the thicker perovskite layer, with respect to that of the thinner one, suggests that it is the asymmetry of the diffusion lengths within the perovskite layer that determines the V_{oc} decrease with the irradiance direction, instead of the PTAA. To confirm this hypothesis, we performed additional DD simulations with varying PTAA thicknesses, showing that for thicknesses > 100 nm, the V_{oc} drop due to PTAA absorption would limit the perovskite-focused analysis (see Figure S11b in the Supporting Information). In contrast, for PTAA thicknesses < 50 nm, it is safe to assume that most of the contribution to the irradiance direction-dependent response is due to the perovskite.

Our experimental observations and numerical simulations suggest that a systematic increase (decrease) in photocurrent and photovoltage occurs for front compared to rear directions of monochromatic irradiance when $L_n \ll L_p$ ($L_n \gg L_p$) in the bulk of the absorber layers whose $w \ll L$ in both directions, in p-i-n devices with transparent electrodes. In general, a dependence on the direction of illumination will show up whenever there is an asymmetry in the respective diffusion lengths of electrons and holes (see below). This is typically the case for transparent solar cells under UV irradiance. Nevertheless, it is strongly recommended to validate these analyses with experiments comparing samples with thinner and thicker absorber layers with the same transport layers since the UV absorption of some of the transport materials (e.g., PTAA) could also contribute to the direction-dependent response.

The above reasoning is better explained with the aid of the energy diagrams in Figure 3a,b that summarize the differences between the front and rear directions of irradiance, respectively, considering the main transport and recombination mechanisms. Regardless of whether the incident photon flux accesses the device through the electron or hole transport material, ETM and HTM, respectively, four main processes take place: (1) photon absorption by electrons with energies smaller than that of the conduction band maximum (E_V); (2) charge carrier generation exciting an electron to energies above the minimum E_C and leaving a hole in the valence band; (3) drift and diffusion of electrons and holes toward the ETM and the HTM, respectively; and (4) charge carrier recombination. These processes are well-known and occur in p-i-n devices as long as there is a built-in field and the diffusion lengths of electrons and holes are different and complementary in the selective contacts. As a result, the drift-diffusion current of electrons and holes, $J_{n,DD}$ and $J_{p,DD}$, in the direction of the built-in field (ξ_{bi}) occur as the charge carriers are extracted toward the ETM and HTM, respectively.

The drift or diffusion contributions to $J_{n,DD}$ or $J_{p,DD}$, and their proportion to the total current $J = J_{n,DD} + J_{p,DD}$, depend on the device architecture and properties, the bias, and incident irradiance. For example, in short-circuit conditions, $J = J_{ph}$ typically has a main contribution from drift current.[38] Importantly, DD current components can also occur in the direction opposite to that of the ξ_{bi} and J_{ph}, which would reduce the performance of the devices (e.g., due to field ion screening).[39−42] However, in the following, we assume these contributions to be independent of the direction of irradiance, meaning that they are already accounted for in $J_{n,DD}$ and $J_{p,DD}$, which are also fundamentally independent of the direction of irradiance.

The introduction of B-L absorption profiles with $w \ll L$ in Figure 3 illustrates how the photogeneration profile cannot be approximated to a homogeneous distribution and diffusion current of electrons ($J_{n,\alpha Diff}$) and holes ($J_{p,\alpha Diff}$) takes place. The absolute values of $J_{n,\alpha Diff}$ and $J_{n,\alpha Diff}$ are assumed to be approximately the same, regardless of the direction of irradiance of monochromatic photons with absorption coefficient α. However, for the front direction of irradiance (Figure 3a), electrons (5a) and holes (5b) diffuse toward the HTM, in the directions against and in favor to the current, respectively. In contrast, in the rear direction of irradiance (Figure 3b), electrons (5c) and holes (5b) diffuse toward the ETM, in the directions in favor and against the current, respectively. Therefore, the current difference between front and rear directions of irradiance can be approximated to

$$\Delta J_{FR} = J_{front} - J_{rear} \approx 2(J_{p,\alpha Diff} - J_{n,\alpha Diff}) \tag{7}$$

An exact solution for expressing eq 7 in terms of the diffusion lengths and other fundamental transport properties may require numerical methods. However, considering (i) an approximation to the solution of the continuity equation for a diffusion process with a monochromatic B-L generation rate at the edge of the depletion region[43] and (ii) the non-homogeneous photogeneration ($w < L$), one can estimate:

$$J_{n,\alpha Diff} = qG(L - w)\left(1 + \frac{w}{L_n}\right)^{-1} \tag{8a}$$

and

$$J_{p,\alpha Diff} = qG(L - w)\left(1 + \frac{w}{L_p}\right)^{-1} \tag{8b}$$

Then, substituting eq 8 into eq 7, it leads to the empirical photocurrent direction difference

$$\Delta J_{FR} = 2qG(L - w)\left(\frac{L_p}{L_p + w} - \frac{L_n}{L_n + w}\right) \tag{9}$$

From eq 9 we can conclude that (i) no current difference depending on the direction of irradiance is obtained for quasi-homogeneous photogeneration ($w > L \Rightarrow \Delta J_{FR} = 0$) or (ii) identical diffusion lengths ($L_n = L_p \Rightarrow \Delta J_{FR} = 0$) and (iii) that the sign of the direction current difference depends on the diffusion lifetimes: $L_p \lessgtr L_n \Rightarrow \Delta J_{FR} \lessgtr 0$. Importantly, not only is $L_p \neq L_n$ required for obtaining a measurable value $\Delta J_{FR} \neq 0$, but also there is a close relation with w. Expression 9 can be further extended to the open-circuit condition, resulting in an empirical photovoltage direction difference

$$\Delta V_{FR} = \frac{mk_BT}{q}\ln\left[2q\frac{G(L - w)}{J_0}\left(\frac{L_p}{L_p + w} - \frac{L_n}{L_n + w}\right)\right] \tag{10}$$

where m is the ideality factor, k_BT/q is the thermal voltage, and J_0 is the dark saturation current of the sample.

The normalized values of eq 9 as a function of the ratios L_p/w and L_n/w are presented in Figure 3c, which clearly equals zero in the diagonal, where $L_n = L_p$. However, for diffusion lengths with values similar to the photon penetration depth (L_n, $L_p \sim w$), smaller differences between L_n and L_p produce

https://doi.org/10.1021/acs.jpclett.4c02364
J. Phys. Chem. Lett. 2024, 15, 10153−10161

higher current direction differences (smaller distance between negative-blue and positive-red regions in Figure 3c). In contrast, for diffusion lengths with values significantly smaller or higher than the photon penetration depth (L_n, $L_p \ll w$ or L_n, $L_p \gg w$), it takes higher differences between L_n and L_p to produce significant current direction differences (white-near-zero areas in Figure 3c).

In summary, this study investigated the impact of the difference between electron and hole diffusion lengths on the direction of UV irradiance in transparent $FAPbBr_3$-based PSCs. The devices were fabricated and optimized by including an Isoneo passivation treatment, which not only increased the device *PCE* but also allowed *AVT* values to be as high as 60% for *LUE* values above 5%. The superior performance of the passivated devices was confirmed through various characterization techniques, suggesting a reduction in the nonradiative recombination compared to the reference nonpassivated samples.

The thickness, illumination spectra, and direction of irradiance were studied and correlated with fundamental electron−hole transport properties. The IS analysis of samples thicker than 150 nm under 365 nm UV irradiance from both the front and rear directions demonstrated significant differences in open-circuit and short-circuit conditions, whereas experiments under white LED illumination did not show such trends. Our numerical simulations and the experimental results suggest that the electrons and holes diffusion lengths in the studied $FAPbBr_3$ transparent samples are smaller than 50 nm and greater than 99 nm, respectively.

A discussion on diffusion transport for Beer−Lambert monochromatic absorption was provided, along with empirical approximations for the photocurrent and photovoltage differences between measurements taken from the front and rear directions of irradiance. The characterization protocol introduced here facilitates the identification of the limiting diffusion length requiring further optimization, not only in semitransparent PSCs but also for solar cells with semitransparent electrodes in general. Moreover, the estimation of L_n, L_p, and their difference, could also be extended to samples with several other absorber layer thicknesses, and extra measurement protocols could be used for contrasting and validating the results.

■ ASSOCIATED CONTENT

Supporting Information

The Supporting Information is available free of charge at https://pubs.acs.org/doi/10.1021/acs.jpclett.4c02364.

Additional experimental details, materials, and methods, including photographs of the samples; performance statistics and stability tests; absorption, transmittance and impedance spectra for different irradiance intensities, spectra and directions; drift-diffusion simulation parameters (PDF)

■ AUTHOR INFORMATION

Corresponding Authors

Osbel Almora − *Department of Electronic, Electric, and Automatic Engineering, Universitat Rovira i Virgili, Tarragona 43007, Spain;* orcid.org/0000-0002-2523-0203; Email: osbel.almora@urv.cat

Fabio Matteocci − *Center for Hybrid and Organic Solar Energy, Department of Electronics Engineering, University of Rome ≪Tor Vergata≫, Roma 00133, Italy;* orcid.org/0000-0001-7893-1356; Email: fabio.matteocci@uniroma2.it

Juan Antonio Anta − *Center for Nanoscience and Sustainable Technologies (CNATS) and Department of Physical, Chemical, and Natural Systems, Universidad Pablo de Olavide, Sevilla 41013, Spain;* orcid.org/0000-0002-8002-0313; Email: anta@upo.es

Authors

Farshad Jafarzadeh − *Center for Hybrid and Organic Solar Energy, Department of Electronics Engineering, University of Rome ≪Tor Vergata≫, Roma 00133, Italy;* orcid.org/0000-0002-6722-9075

Mohamed Samir − *Department of Electronic, Electric, and Automatic Engineering, Universitat Rovira i Virgili, Tarragona 43007, Spain*

Renán Escalante − *Center for Nanoscience and Sustainable Technologies (CNATS) and Department of Physical, Chemical, and Natural Systems, Universidad Pablo de Olavide, Sevilla 41013, Spain;* orcid.org/0000-0002-5100-5448

Diego Di Girolamo − *Center for Hybrid and Organic Solar Energy, Department of Electronics Engineering, University of Rome ≪Tor Vergata≫, Roma 00133, Italy;* orcid.org/0000-0001-6307-1138

Jessica Barichello − *Center for Hybrid and Organic Solar Energy, Department of Electronics Engineering, University of Rome ≪Tor Vergata≫, Roma 00133, Italy;* orcid.org/0000-0003-1277-4217

Francesca Brunetti − *Center for Hybrid and Organic Solar Energy, Department of Electronics Engineering, University of Rome ≪Tor Vergata≫, Roma 00133, Italy;* orcid.org/0000-0003-2287-4545

Lluis F. Marsal − *Department of Electronic, Electric, and Automatic Engineering, Universitat Rovira i Virgili, Tarragona 43007, Spain;* orcid.org/0000-0002-5976-1408

Complete contact information is available at: https://pubs.acs.org/10.1021/acs.jpclett.4c02364

Notes

The authors declare no competing financial interest.

■ ACKNOWLEDGMENTS

J.A.A. acknowledges the Ministerio de Ciencia e Innovación of Spain, Agencia Estatal de Investigación (AEI), and EU (FEDER) under grants TED2021-129758B−C33 (TransEL) and PID2022-140061OB-I00 (DEEPMATSOLAR). O.A. acknowledges the Juan de la Cierva Fellowship grant FJC2021-046887-I funded by MICIU/AEI/10.13039/501100011033 and by the European Union NextGenerationEU/PRTR. F.M acknowledges Horizon 2020 research and innovation program under Grant Agreement no. 101007084 (CITYSOLAR) and F.B acknowledges the European Union's Horizon 2020 Research and Innovation Program under grant agreement no. 763989 (APOLO).

■ REFERENCES

(1) Almora, O.; Cabrera, C. I.; Erten-Ela, S.; Forberich, K.; Fukuda, K.; Guo, F.; Hauch, J.; Ho-Baillie, A. W. Y.; Jacobsson, T. J.; Janssen, R. A. J.; Kirchartz, T.; Loi, M. A.; Mathew, X.; Mitzi, D. B.; Nazeeruddin, M. K.; Paetzold, U. W.; Rand, B. P.; Rau, U.; Someya,

T.; Unger, E.; Vaillant-Roca, L.; Brabec, C. J. Device Performance of Emerging Photovoltaic Materials (Version 4). *Adv. Energy Mater.* **2024**, *14*, 2303173.
(2) Lee, K.; Um, H.-D.; Choi, D.; Park, J.; Kim, N.; Kim, H.; Seo, K. The Development of Transparent Photovoltaics. *Cell Rep. Phys. Sci.* **2020**, *1*, No. 100143.
(3) Yu, H.; Wang, J.; Zhou, Q.; Qin, J.; Wang, Y.; Lu, X.; Cheng, P. Semi-transparent organic photovoltaics. *Chem. Soc. Rev.* **2023**, *52*, 4132−4148.
(4) Grifoni, F.; Bonomo, M.; Naim, W.; Barbero, N.; Alnasser, T.; Dzeba, I.; Giordano, M.; Tsaturyan, A.; Urbani, M.; Torres, T.; Barolo, C.; Sauvage, F. Toward Sustainable, Colorless, and Transparent Photovoltaics: State of the Art and Perspectives for the Development of Selective Near-Infrared Dye-Sensitized Solar Cells. *Adv. Energy Mater.* **2021**, *11*, No. 2101598.
(5) Patel, M.; Bhatnagar, P.; Lee, J.; Kumar, N.; Nguyen, T. T.; Kim, J. Transparent photovoltaic window for visible light communications with onsite power and reliable machine learning features. *Nano Energy* **2023**, *115*, No. 108696.
(6) Zhu, Y.; Shu, L.; Fan, Z. Recent Progress on Semi-transparent Perovskite Solar Cell for Building-integrated Photovoltaics. *Chem. Res. Chin. Univ.* **2020**, *36*, 366−376.
(7) Gorjian, S.; Bousi, E.; Özdemir, Ö.E.; Trommsdorff, M.; Kumar, N. M.; Anand, A.; Kant, K.; Chopra, S. S. Progress and challenges of crop production and electricity generation in agrivoltaic systems using semi-transparent photovoltaic technology. *Renew. Sust. Energy Rev.* **2022**, *158*, No. 112126.
(8) Mamun, M. A. A.; Dargusch, P.; Wadley, D.; Zulkarnain, N. A.; Aziz, A. A. A review of research on agrivoltaic systems. *Renew. Sust. Energy Rev.* **2022**, *161*, No. 112351.
(9) Pulli, E.; Rozzi, E.; Bella, F. Transparent photovoltaic technologies: Current trends towards upscaling. *Energy Conversion and Management* **2020**, *219*, No. 112982.
(10) Wang, H.; Lin, C.; Hu, Y.; Zhang, X.; Han, J.; Cheng, Y. Study on indoor adaptive thermal comfort evaluation method for buildings integrated with semi-transparent photovoltaic window. *Building Environ.* **2023**, *228*, No. 109834.
(11) Yang, C.; Liu, D.; Lunt, R. R. How to Accurately Report Transparent Luminescent Solar Concentrators. *Joule* **2019**, *3*, 2871−2876.
(12) Kothandaraman, R. K.; Jiang, Y.; Feurer, T.; Tiwari, A. N.; Fu, F. Near-Infrared-Transparent Perovskite Solar Cells and Perovskite-Based Tandem Photovoltaics. *Small Methods* **2020**, *4*, 2000395.
(13) Jafarzadeh, F.; Castriotta, L. A.; Legrand, M.; Ory, D.; Cacovich, S.; Skafi, Z.; Barichello, J.; De Rossi, F.; Di Giacomo, F.; Di Carlo, A.; Brown, T.; Brunetti, F.; Matteocci, F. Flexible, Transparent, and Bifacial Perovskite Solar Cells and Modules Using the Wide-Band Gap $FAPbBr_3$ Perovskite Absorber. *ACS Appl. Mater. Interfaces* **2024**, *16*, 17607−17616.
(14) Zhang, Y.; Liang, Y.; Wang, Y.; Guo, F.; Sun, L.; Xu, D. Planar $FAPbBr_3$ Solar Cells with Power Conversion Efficiency above 10%. *ACS Energy Lett.* **2018**, *3*, 1808−1814.
(15) Di Girolamo, D.; Vidon, G.; Barichello, J.; Di Giacomo, F.; Jafarzadeh, F.; Paci, B.; Generosi, A.; Kim, M.; Castriotta, L. A.; Frégnaux, M.; Guillemoles, J.-F.; Brunetti, F.; Schulz, P.; Ory, D.; Cacovich, S.; Di Carlo, A.; Matteocci, F. Breaking 1.7 V Open Circuit Voltage in Large Area Transparent Perovskite Solar Cells Using Interfaces Passivation. *Adv. Energy Mater.* **2024**, *14*, No. 2400663.
(16) Wu, Z.; Bi, E.; Ono, L. K.; Li, D.; Bakr, O. M.; Yan, Y.; Qi, Y. Passivation strategies for enhancing device performance of perovskite solar cells. *Nano Energy* **2023**, *115*, No. 108731.
(17) Liu, Y.; Kim, B. J.; Wu, H.; Boschloo, G.; Johansson, E. M. J. Efficient and Stable $FAPbBr_3$ Perovskite Solar Cells via Interface Modification by a Low-Dimensional Perovskite Layer. *ACS Appl. Energy Mater.* **2021**, *4*, 9276−9282.
(18) Babayigit, A.; Ethirajan, A.; Muller, M.; Conings, B. Toxicity of organometal halide perovskite solar cells. *Nat. Mater.* **2016**, *15*, 247−251.
(19) Schileo, G.; Grancini, G. Lead or no lead? Availability, toxicity, sustainability and environmental impact of lead-free perovskite solar cells. *J. Mater. Chem. C* **2021**, *9*, 67−76.
(20) Goetz, K. P.; Taylor, A. D.; Hofstetter, Y. J.; Vaynzof, Y. Sustainability in Perovskite Solar Cells. *ACS Appl. Mater. Interfaces* **2021**, *13*, 1−17.
(21) Ding, G.; Zheng, Y.; Xiao, X.; Cheng, H.; Zhang, G.; Shi, Y.; Shao, Y. Sustainable development of perovskite solar cells: keeping a balance between toxicity and efficiency. *Journal of Materials Chemistry A* **2022**, *10*, 8159−8171.
(22) Yang, C.; Liu, D.; Bates, M.; Barr, M. C.; Lunt, R. R. How to Accurately Report Transparent Solar Cells. *Joule* **2019**, *3*, 1803−1809.
(23) Traverse, C. J.; Pandey, R.; Barr, M. C.; Lunt, R. R. Emergence of highly transparent photovoltaics for distributed applications. *Nature Energy* **2017**, *2*, 849−860.
(24) Kumar, P.; Shankar, G.; Pradhan, B. Recent progress in bifacial perovskite solar cells. *Appl. Phys. A: Mater. Sci. Process.* **2023**, *129*, 63.
(25) Einstein, A. Über die von der molekularkinetischen Theorie der Wärme geforderte Bewegung von in ruhenden Flüssigkeiten suspendierten Teilchen. *Annalen der Physik* **1905**, *322*, 549−560.
(26) Nelson, J. *The Physics of Solar Cells*; Imperial College Press: Singapore, 2003.
(27) Tokmoldin, N.; Hosseini, S. M.; Raoufi, M.; Phuong, L. Q.; Sandberg, O. J.; Guan, H.; Zou, Y.; Neher, D.; Shoaee, S. Extraordinarily long diffusion length in PM6:Y6 organic solar cells. *J. Mater. Chem. A* **2020**, *8*, 7854−7860.
(28) Hodes, G.; Kamat, P. V. Understanding the Implication of Carrier Diffusion Length in Photovoltaic Cells. *J. Phys. Chem. Lett.* **2015**, *6*, 4090−4092.
(29) Halme, J.; Miettunen, K.; Lund, P. Effect of Nonuniform Generation and Inefficient Collection of Electrons on the Dynamic Photocurrent and Photovoltage Response of Nanostructured Photoelectrodes. *J. Phys. Chem. C* **2008**, *112*, 20491−20504.
(30) Almora, O.; Cabrera, C. I.; Garcia-Cerrillo, J.; Kirchartz, T.; Rau, U.; Brabec, C. J. Quantifying the Absorption Onset in the Quantum Efficiency of Emerging Photovoltaic Devices. *Adv. Energy Mater.* **2021**, *11*, No. 2100022.
(31) Ghahremanirad, E.; Almora, O.; Suresh, S.; Drew, A. A.; Chowdhury, T. H.; Uhl, A. R. Beyond Protocols: Understanding the Electrical Behavior of Perovskite Solar Cells by Impedance Spectroscopy. *Adv. Energy Mater.* **2023**, *13*, No. 2204370.
(32) Alvarez, A. O.; Ravishankar, S.; Fabregat-Santiago, F. Combining Modulated Techniques for the Analysis of Photosensitive Devices. *Small Methods* **2021**, *5*, No. 2100661.
(33) Almora, O.; Zhao, Y.; Du, X.; Heumueller, T.; Matt, G. J.; Garcia-Belmonte, G.; Brabec, C. J. Light Intensity Modulated Impedance Spectroscopy (LIMIS) in All-Solid-State Solar Cells at Open-Circuit. *Nano Energy* **2020**, *75*, No. 104982.
(34) Snaith, H. J.; Abate, A.; Ball, J. M.; Eperon, G. E.; Leijtens, T.; Noel, N. K.; Stranks, S. D.; Wang, J.T.-W.; Wojciechowski, K.; Zhang, W. Anomalous Hysteresis in Perovskite Solar Cells. *J. Phys. Chem. Lett.* **2014**, *5*, 1511−1515.
(35) Rau, U.; Blank, B.; Müller, T. C. M.; Kirchartz, T. Efficiency Potential of Photovoltaic Materials and Devices Unveiled by Detailed-Balance Analysis. *Phys. Rev. Appl.* **2017**, *7*, No. 044016.
(36) Swinehart, D. F. The Beer-Lambert Law. *J. Chem. Educ.* **1962**, *39*, 333.
(37) Almora, O.; Miravet, D.; Matt, G. J.; Garcia-Belmonte, G.; Brabec, C. J. Analytical Model for Light Modulating Impedance Spectroscopy (LIMIS) in All-Solid-State p-n Junction Solar Cells at Open-Circuit. *Appl. Phys. Lett.* **2020**, *116*, No. 013901.
(38) Almora, O.; López-Varo, P.; Escalante, R.; Mohanraj, J.; Marsal, L. F.; Olthof, S.; Anta, J. A. Instability Analysis of Perovskite Solar Cells via Short-Circuit Impedance Spectroscopy: A case study on NiO_x passivation. *J. Appl. Phys.* **2024**, *136*, No. 094502.
(39) Thiesbrummel, J.; Shah, S.; Gutierrez-Partida, E.; Zu, F.; Peña-Camargo, F.; Zeiske, S.; Diekmann, J.; Ye, F.; Peters, K. P.; Brinkmann, K. O.; Caprioglio, P.; Dasgupta, A.; Seo, S.; Adeleye, F. A.; Warby, J.; Jeangros, Q.; Lang, F.; Zhang, S.; Albrecht, S.; Riedl, T.;

https://doi.org/10.1021/acs.jpclett.4c02364
J. Phys. Chem. Lett. 2024, 15, 10153−10161

Armin, A.; Neher, D.; Koch, N.; Wu, Y.; Le Corre, V. M.; Snaith, H.; Stolterfoht, M. Ion-induced field screening as a dominant factor in perovskite solar cell operational stability. *Nat. Energy* **2024**, *9*, 664−676.
(40) Álvarez, A. O.; Lédée, F.; García-Batlle, M.; López-Varo, P.; Gros-Daillon, E.; Mayén Guillén, J.; Verilhac, J.-M.; Lemercier, T.; Zaccaro, J.; Marsal, L. F.; Garcia-Belmonte, G.; Almora, O. Ionic field screening in $MAPbBr_3$ crystals from remnant sensitivity in X-ray detection. *ACS Phys. Chem. Au* **2023**, *3*, 386−393.
(41) Moia, D.; Gelmetti, I.; Calado, P.; Hu, Y.; Li, X.; Docampo, P.; de Mello, J.; Maier, J.; Nelson, J.; Barnes, P. R. F. The dynamics of internal electric field screening in hybrid perovskite solar cells probed using electroabsorption. *Phys. Rev. Appl.* **2022**, *18*, No. 044056.
(42) Almora, O.; Miravet, D.; Gelmetti, I.; Garcia-Belmonte, G. Long-term Field Screening by Mobile Ions in Thick Metal Halide Perovskites: Understanding Saturation Currents. *Phys. Status Solidi RRL* **2022**, *16*, No. 202200336.
(43) Fahrenbruch, A. L.; Bube, R. H. *Fundamentals of Solar Cells*; Photovoltaic Solar Energy Conversion, Academic Press: New York, 1983.

https://doi.org/10.1021/acs.jpclett.4c02364
J. Phys. Chem. Lett. 2024, 15, 10153−10161